Single-Phase and Two-Phase Hybrid Cooling Schemes for High-Heat-Flux Thermal Management of Defense Electronics

Myung Ki Sung

Issam Mudawar[1]
e-mail: mudawar@ecn.purdue.edu

Boiling and Two-Phase Flow Laboratory (BTPFL),
Purdue University International Electronic
Cooling Alliance (PUIECA),
Mechanical Engineering Building,
585 Purdue Mall,
West Lafayette, IN 47907-2088

This study examines the cooling performance of two hybrid cooling schemes that capitalize on the merits of both microchannel flow and jet impingement to achieve the high cooling fluxes and uniform temperatures demanded by advanced defense electronics. The jets supply HFE 7100 liquid coolant gradually into each microchannel. The cooling performances of two different jet configurations, a series of circular jets and a single slot jet, are examined both numerically and experimentally. The single-phase performances of both configurations are accurately predicted using 3D numerical simulation. Numerical results point to complex interactions between the jets and the microchannel flow, and superior cooling performance is achieved by optimal selection of microchannel height. The two-phase cooling performance of the circular-jet configuration is found superior to that of the slot jet, especially in terms of high-flux heat dissipation. Unprecedented cooling fluxes, as high as 1127 W/cm^2, are achieved with the circular jets without incurring CHF. [DOI: 10.1115/1.3111253]

1 Introduction

High-flux thermal management is a primary design concern for advanced defense devices found in radars, directed-energy laser and microwave weapon systems, and avionics. While these devices follow the trend of escalating power density of commercial electronics, heat fluxes from defense devices are now projected to exceed 1000 W/cm^2 [1]. This level of heat dissipation exceeds the capabilities of today's most advanced dielectric liquid cooling systems, single-phase or two-phase, which points to an urgent need to develop new powerful cooling solutions.

In pursuing such cooling solutions, it is useful to examine the attributes of today's most effective cooling schemes. Those schemes are based mostly on two types of coolant flows, microchannel and jet impingement. Small hydraulic diameter greatly increases the convective heat transfer coefficient in microchannels. Microchannel heat sinks also feature small size and weight, and require minimal coolant inventory. Two key drawbacks of microchannel heat sinks are high pressure drop and large temperature gradients along the direction of coolant flow. Jet impingement produces enormous heat transfer coefficients in the impingement zone and generally require smaller pressure drop than microchannels. However, they also produce large surface temperature gradients away from the impingement zone. To diffuse this concentrated cooling effect, multiple jets are preferred for high-flux heat removal, especially from large surface areas. However, this greatly increases the coolant's flow rate and complicates the routing of spent coolant within the cooling module. Clearly, both microchannel flow and jet impingement are good candidates for high-flux heat removal, but they also pose practical challenges.

Microchannel heat sinks have been investigated both experimentally [2–7] and numerically [8–10]. Tuckerman and Pease [2] demonstrated the effectiveness of single-phase microchannel heat sinks by dissipating up to 790 W/cm^2 with water. Bowers and Mudawar [4] achieved 3000 W/cm^2 and 27,000 W/cm^2 with single-phase and two-phase flow, respectively, with water flow in microtubes. However, because of poor thermophysical properties, cooling heat fluxes are far smaller for the dielectric coolants permissible in electronics cooling applications.

Single-phase and two-phase jet-impingement cooling have been the subjects of intense study for many decades. Numerical methods have been quite effective at modeling the single-phase cooling behavior of jets [11–13], however, most published jet studies are experimental [14–21]. Wadsworth and Mudawar [17] conducted confined multiple slot-jet impingement experiments using FC-72 as working fluid and developed a superpositioning technique to correlate single-phase heat transfer coefficient data. Wolf et al. [19] experimentally demonstrated that the two-phase heat transfer coefficient is independent of jet velocity in the nucleate boiling region. Monde [16] identified different critical heat flux (CHF) regimes corresponding to different flow rates and system pressures for circular impingement jets. Monde and Mitsutake [21] extended these findings to multiple circular jets.

Aside from dissipating the heat, a thermal management system must maintain the device's temperature below a limit that is dictated by material and reliability concerns. This task becomes increasingly more challenging with high-flux devices, and the coolant's temperature must decrease greatly with the aid of a refrigeration cycle in order to meet this temperature constraint.

Recently, the authors of the present study proposed combining the cooling merits of microchannel flow and jet-impingement using a "hybrid" cooling module [22,23]. Aside from capitalizing on the merits of the two cooling schemes, a hybrid module also serves to eliminate their drawbacks. The coolant is introduced gradually in the form of slot jets or circular jets into microchannels, thereby taking advantage of the high-heat-flux removal capabilities of both jet impingement and microchannel flow while decreasing both the temperature gradients along the microchannel

[1]Corresponding author.

Contributed by the Electrical and Electronic Packaging Division of ASME for publication in the JOURNAL OF ELECTRONIC PACKAGING. Manuscript received July 1, 2008; final manuscript received January 8, 2009; published online April 21, 2009. Assoc. Editor: Bernard Courtois. Paper presented at the Itherm 2008.

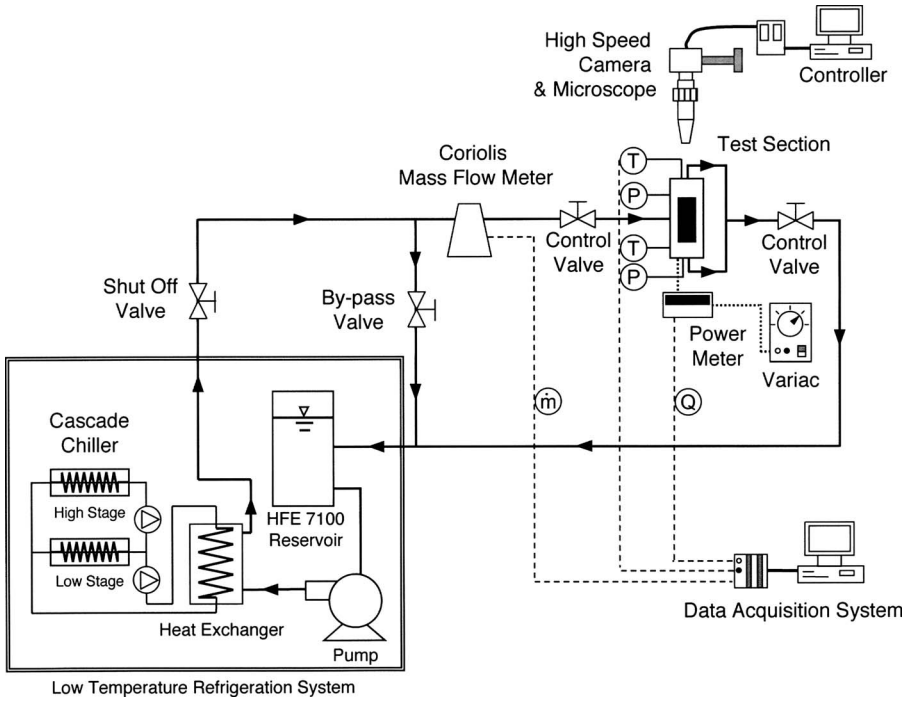

Fig. 1 Schematic of flow control system

and pressure drop, and better controlling the flow of spent fluid downstream of the impingement zones of the jets.

This paper provides new findings concerning the single-phase and two-phase cooling performances of hybrid cooling modules for high performance defense electronics. Two different hybrid configurations are tested. The first consists of supplying the coolant from a single slot jet facing the center of each microchannel. The second involves depositing coolant gradually from a series of circular microjets facing the entire length of the microchannel. The single-phase cooling performance of each module is examined both numerically and experimentally using HFE 7100 as working fluid. The two-phase cooling characteristics and CHF trends are explored experimentally. To enhance cooling performance, the temperature of HFE 7100 is greatly reduced with the aid of an indirect refrigeration cooling system. The two hybrid cooling modules are evaluated relative to the magnitude of the heat transfer coefficient, surface temperature uniformity, and upper heat flux limit.

2 Experimental Methods

2.1 Flow Loop. Figure 1 shows a schematic diagram of a flow control system that is configured to supply low temperature HFE 7100 liquid coolant to the hybrid cooling module at controlled flow rate, pressure, and temperature. This system consists of two separate loops: a primary HFE 7100 loop that contains the test module, and an indirect refrigeration loop that is coupled to the primary loop via a heat exchanger. Aside from the test module, the primary loop contains a reservoir, a centrifugal pump, and a Coriolis flow meter. Flow rate and outlet pressure are controlled by two throttling values situated upstream and downstream of the test module, as well as a bypass valve. The refrigeration loop uses feedback control to regulate the temperature of HFE 7100 liquid exiting the heat exchanger to within $\pm 0.5^\circ$C.

2.2 Test Module. Figure 2 shows the test module consists of a copper block, a microjet plate, upper and bottom G-11 fiberglass plastic housings, and 16 cartridge heaters. Five 1 mm wide and 3 mm deep microchannels are cut equidistantly within the 1 cm width of the top 1.0×2.0 cm^2 test surface area of the copper block. The "microchannel" designation adopted in this study corresponds to the 1 mm channel width, which is the channel dimension responsible for restricting the motion of departing bubbles, as opposed to hydraulic diameter. The cartridge heaters are inserted into bores in the underside of the copper block. Electrical power is supplied to the cartridge heaters from a variable voltage transformer, and power input is measured by a Yokogawa WT 210 wattmeter. Notice that the top portion of the copper block is tapered in two steps to ensure uniform temperature across the test surface. The height of each step is guided by 3D numerical simulation of heat conduction within the copper block. Four type-T thermocouples are inserted beneath the bottom wall of the central microchannel to monitor streamwise temperature variations.

As shown in Fig. 2, coolant entering the test module first stagnates in a plenum in the underside of the upper housing, from where it flows through circular or rectangular orifices in the microjet copper plate. The jets impinge inside the microchannels and the flow is divided equally, with each part flowing to one of two outlet plenums in the bottom housing. An absolute pressure transducer and a type-T thermocouple are connected to the upstream plenum. A second pressure transducer is connected to one of the outlet plenums and a type-T thermocouple to the other outlet plenum.

Two 1.65 mm thick jet plates are used to produce the two jet configurations. The first contains five parallel 0.6 mm wide and 2.94 mm long slots that are machined equidistantly, facing the microchannels in the copper block. The circular-jet plate has 5 parallel arrays of 14 0.39 mm diameter circular holes drilled equidistantly within a 1 cm width. Figure 3 shows details of unit cells representing the circular-jet plate and the slot-jet plate. Key dimensions of each configuration are provided in Table 1. Notice that the total flow area is the same for both configurations. Figure 3 helps illustrate a fundamental difference between the two jet configurations. While the circular jets supply the coolant gradually along the entire length of the microchannel, the slot jet supplies the coolant in a more concentrated fashion toward the center of the microchannel.

Measurement uncertainties associated with the pressure trans-

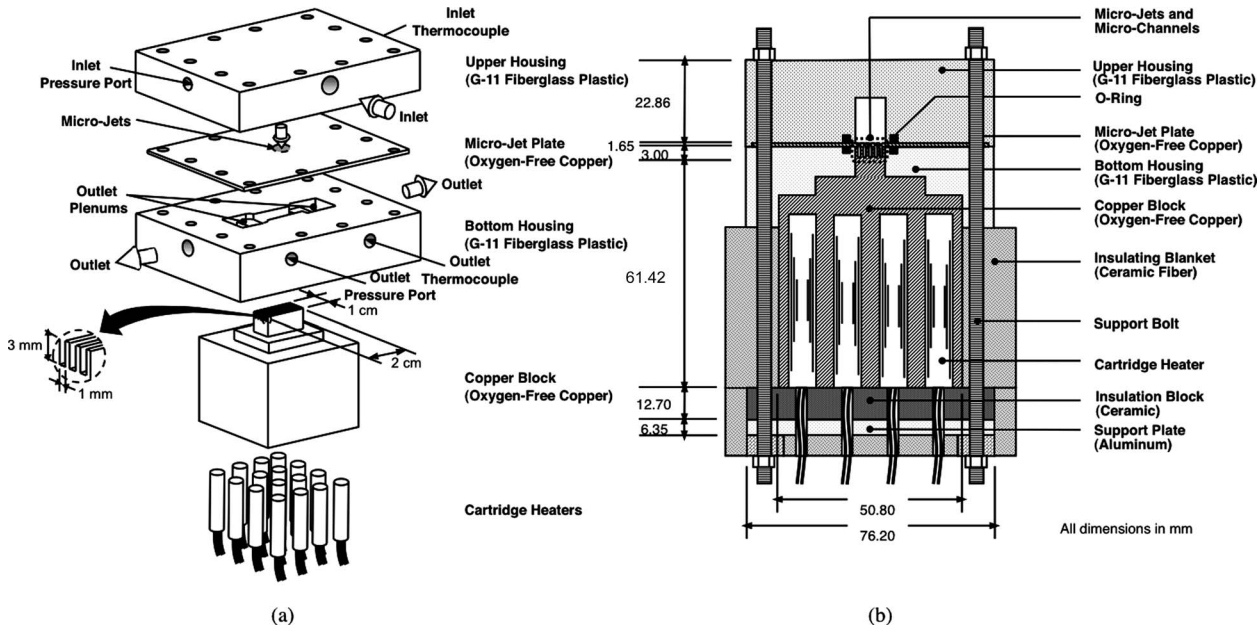

Fig. 2 (*a*) Test module construction and (*b*) cross section of module assembly

ducers, flow meter, wattmeter, and thermocouples are 0.5%, 0.1%, 0.5%, and 0.3°C, respectively. A numerical 3D model of the test module yielded a worst-case heat loss (corresponding to the lowest coolant flow rate tested) of less than 8% of the electrical power input. The heat fluxes presented in this study are therefore based on the measured electrical power input. The experimental operating conditions are listed in Table 2. Table 3 provides saturated thermophysical properties of HFE 7100 at 1.0 bar. Additional details on the experimental methods used in the present study can be found in Ref. [23].

3 Single-Phase Heat Transfer Results

3.1 Microchannel Height Effects. Microchannel height plays a significant role in hybrid microchannel/jet-impingement cooling systems. This height represents the thickness of liquid that a jet must penetrate before impacting the microchannel's bottom wall. The effects of microchannel height on surface temperature and spatial temperature gradients are investigated numerically for HFE 7100 circular jets at two jet velocities, 1 m/s and 5 m/s; jet diameter and microchannel width are fixed at 0.39 mm and 1 mm,

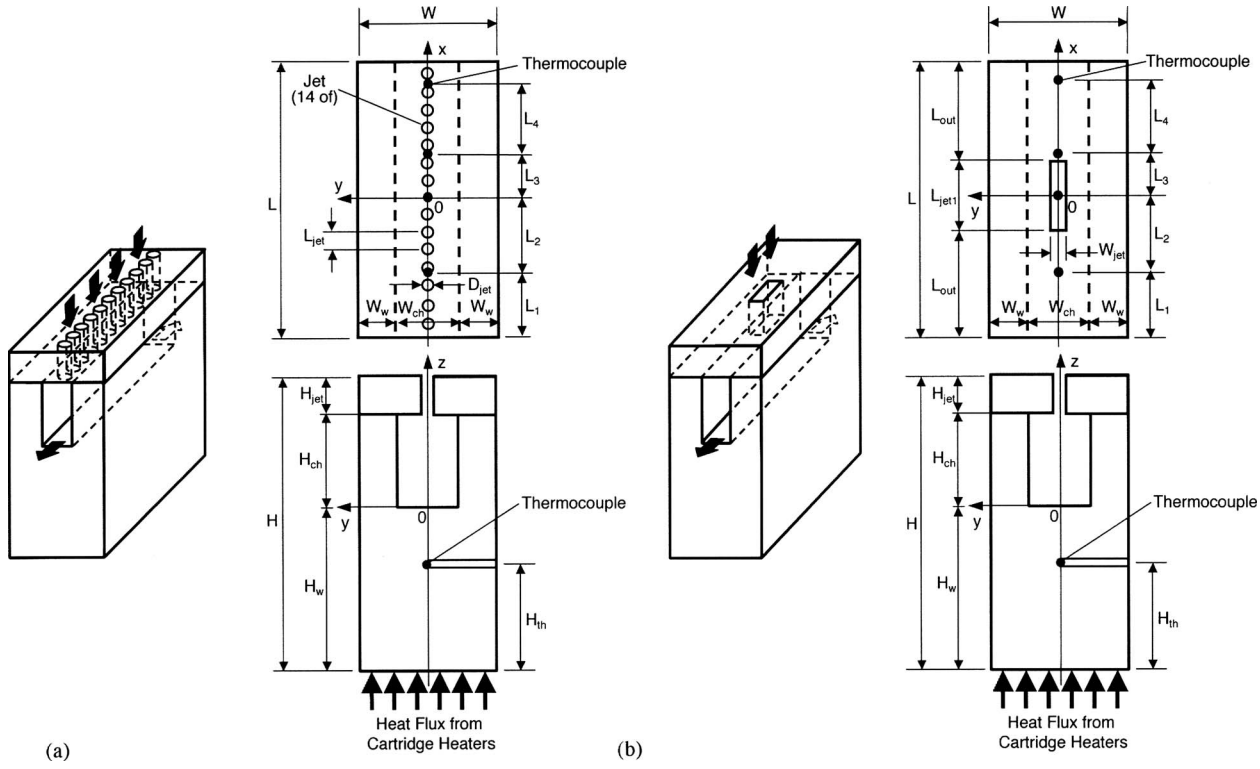

Fig. 3 Schematics of unit cells for (*a*) circular jets and (*b*) slot jet

Table 1 Dimensions of unit cells

Jet types	L (mm)	L_1 (mm)	L_2 (mm)	L_3 (mm)	L_4 (mm)	W (mm)
Circular	20.00	4.00	6.00	3.00	6.00	1.83
Slot	20.00	4.00	6.00	3.00	6.00	1.83
	W_{ch} (mm)	W_w (mm)	H (mm)	H_{jet} (mm)	H_{ch} (mm)	H_w (mm)
Circular	1.00	0.42	14.27	1.65	3.00	7.62
Slot	1.00	0.42	14.27	1.65	3.00	7.62
	H_{th} (mm)	D_{jet} (mm)	L_{jet} (mm)	W_{jet} (mm)	L_{jet1} (mm)	
Circular	5.08	0.39	1.43			
Slot	5.08			0.60	2.94	

respectively. FLUENT 6.2.16 [24] and GAMBIT 2.2.30 [25] are used to predict the 3D flow field and heat transfer characteristics for both hybrid schemes. The governing conservation equations are solved for steady, turbulent, and incompressible flow with constant properties. The standard two-equation k-ε turbulence model [26] is applied for closure of the Reynolds stress tensor. Details concerning the boundary conditions and mesh size are discussed in a previous paper by the authors [23].

Table 2 Experimental operating conditions

Working fluid	Inlet temperature T_{in} (°C)	Inlet flow rate $Q\times10^{-6}$(m^3/s)	Effective heat flux q''_{eff} (W/cm^2)
HFE 7100	−40 to 20	6.82 to 45.5	16.1 to 304.9

Table 3 Summary of saturated thermophysical properties of HFE 7100 at 1.0 bar

T_{sat} (°C)	h_{fg} (kJ/kg)	ρ_f (kg/m^3)	ρ_g (kg/m^3)	σ (mN/m)	μ_f (kg/m s)
59.63	111.7	1372.7	9.58	15.7	8.26×10^{-4}

Figures 4(a) and 4(b) show velocity fields for the circular-jet case for H_{ch}=1 mm corresponding to U_{jet}=1 and 5 m/s, respectively. For the lower jet velocity, H_{jet}=1 m/s, upstream jets (near the center of the microchannel) are able to penetrate the microchannel liquid layer and to produce an impingement effect. However, the downstream jets are barely able to penetrate the liquid layer because of a streamwise increase in the velocity of the liquid layer. At the higher jet velocity, U_{jet}=5 m/s, more jets are able to penetrate the liquid layer. Shown in Fig. 4(a) are axial variations of the microchannel's bottom wall temperature for two microchannel heights, H_{ch}=1 and 3 mm. Contrary to intuition, the larger height achieves lower wall temperatures. This can be explained by (1) the significant contribution of microchannel flow to the overall heat transfer process (i.e., as compared with jet impingement) for low jet velocities, and (2) the increased microchannel surface area for H_{ch}=3 mm compared with H_{ch}=1 mm. For U_{jet}=5 m/s, Fig. 4(b) proves heat transfer is far more dominated by jet impingement than by microchannel flow, and the added microchannel heat transfer area for H_{ch}=3 mm is negated by the added resistance to jet penetration. Notice also how streamwise changes in jet penetration for H_{ch}=1 mm are reflected in appreciable temperature gradients compared with H_{ch}=3 mm; such gradients are undesirable in electronics cooling. Recall that the primary goal of the hybrid cooling scheme is to achieve the lowest wall temperature corresponding to the smallest temperature gradients. Figure 4(b) proves that H_{ch}=3 mm is preferred to H_{ch}=1 mm.

Figures 5(a) and 5(b) depict for the circular-jet case velocity fields for H_{ch}=6 mm corresponding to U_{jet}=1 m/s and U_{jet}=5 m/s, respectively. Again, high jet velocity ensures deeper penetration of jets through the liquid layer. Figure 5(a) proves, for U_{jet}=1 m/s, heat transfer is dominated by microchannel flow. Increasing H_{ch} from 3 mm to 6 mm reduces wall temperature by increasing the surface area available for microchannel flow. However, unlike Fig. 4(a), the magnitude of the temperature reduction is comparatively small. This can be explained by the loss of side-

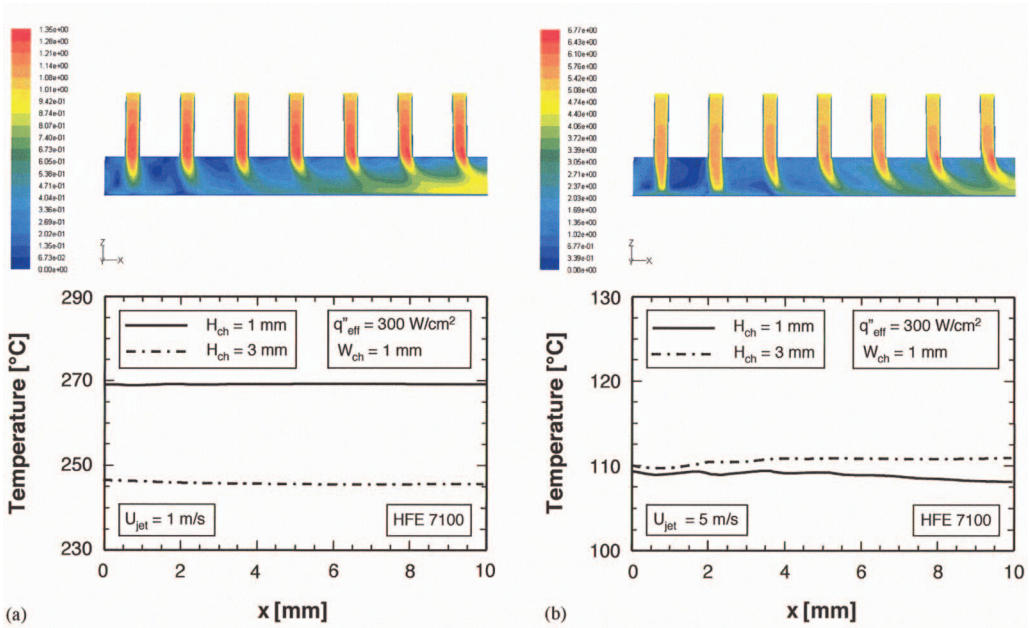

Fig. 4 Numerical predictions of coolant velocity for H_{ch}=1 mm and microchannel bottom wall temperature for H_{ch}=1 and 3 mm along the centerline of microchannel for (*a*) U_{jet}=1 m/s and (b) U_{jet}=5 m/s

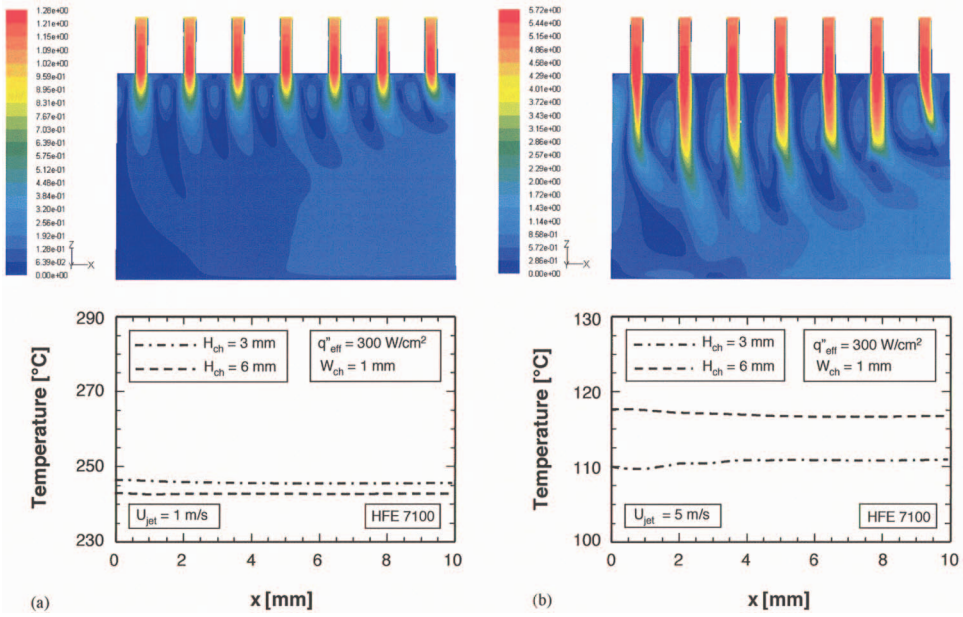

Fig. 5 Numerical predictions of coolant velocity for H_{ch}=6 mm and microchannel bottom wall temperature for H_{ch}=3 and 6 mm along the centerline of microchannel for (*a*) U_{jet}=1 m/s and (*b*) U_{jet}=5 m/s

wall "fin" effectiveness for H_{ch}=6 mm. For U_{jet}=5 m/s, Fig. 5(*b*) shows jet influence is greatly compromised for H_{ch}=6 mm, and far lower wall temperatures are achieved with H_{ch}=3 mm compared with H_{ch}=6 mm. There results, along with those from Fig. 4, prove an intermediate microchannel height of H_{ch}=3 mm provides the best overall thermal performance. This is why this height was used throughout the experimental portion of the present study. This height was also used with the slot-jet configuration for consistency in comparing thermal performance results.

3.2 Single-Phase Experimental Results. Figures 6(*a*) and 6(*b*) show thermocouple readings of the copper block versus jet Reynolds number, Re_{jet}, for the circular jets and slot jet, respectively. For both hybrid cooling configurations, temperatures in the copper block decrease with increasing Re_{jet} for fixed values of q''_{eff} and T_{in}. Figure 6(*a*) shows both the copper block temperatures and gradients between the four thermocouples decrease with decreasing T_{in}. Unlike Fig. 6(*a*), Fig. 6(*b*) shows the variation of thermocouple to inlet temperature difference with the Reynolds number and flow rate. Figure 6(*b*) shows the temperatures and temperature gradients' increase with increasing q''_{eff} and decrease with decreasing T_{in}. Nonetheless, both figures depict very small axial temperature variations for both the circular jets and the slot jet. This illustrates the effectiveness of both hybrid cooling configurations at maintaining surface temperature uniformity.

Figure 7 shows the variation in pressure drop, measured between the inlet and outlet plenums of the test module, with Re_{jet}. Figure 7(*a*) shows pressure drop for the slot jet increases with increasing Re_{jet} but decreases with increasing heat flux. The latter trend is closely related to the lower liquid viscosity at higher temperatures. Figure 7(*b*) shows, for equal Re_{jet}, lower pressure drop is encountered with the slot-jet compared with the circular jets. This can be explained by stronger contraction and expansion effects, and smaller diameter of the circular jets.

3.3 Comparison of Single-Phase Cooling Performances of Two Hybrid Cooling Configurations. Numerical simulation is used to predict and compare the cooling performances of the two hybrid cooling configurations. Aside from the copper block temperature results in Fig. 6, temperature variations along the microchannel sidewalls provide important insight into the cooling performance of each hybrid configuration. Figures 8(*a*) and 8(*b*) show sidewall temperature distributions for circular jets at q''_{eff} =162.15 W/cm² and $Q=3.71\times10^{-5}$ m³/s, and slot jets at q''_{eff}

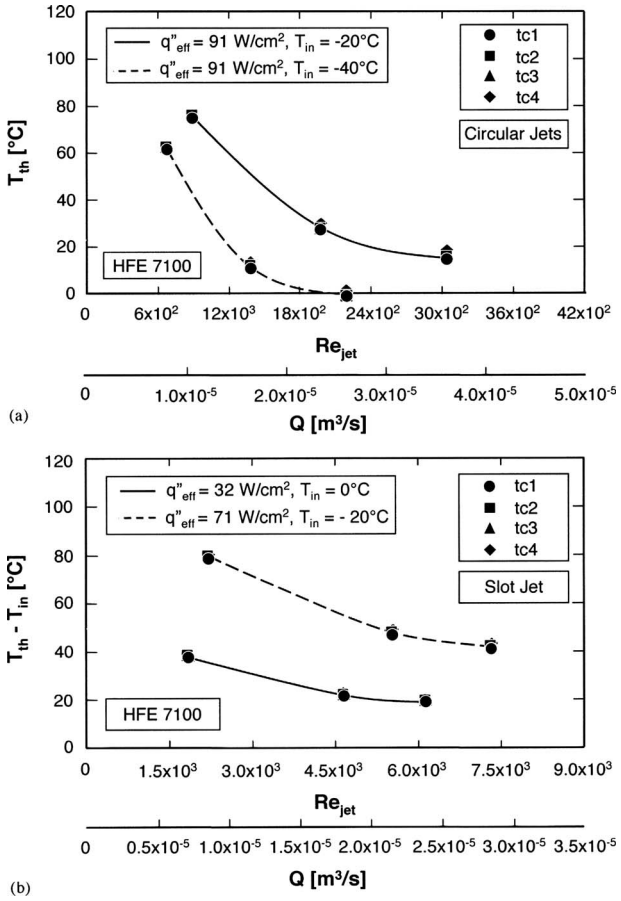

Fig. 6 Thermocouple readings inside heater block versus jet Reynolds number for (*a*) circular jets and (*b*) slot jet

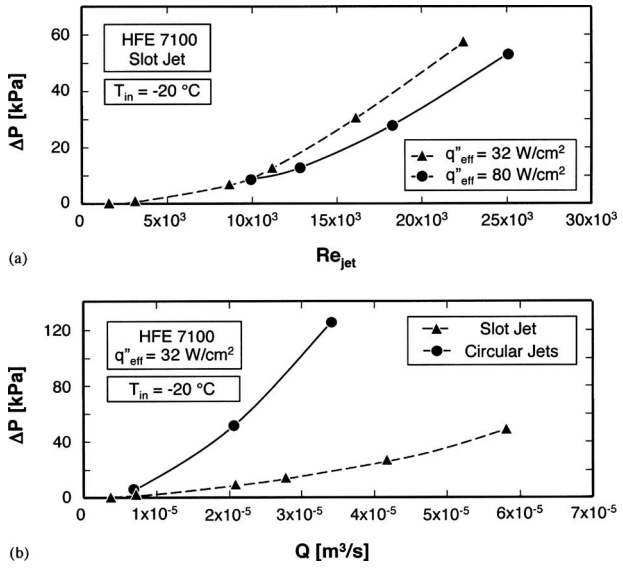

Fig. 7 (*a*) Slot-jet pressure drop versus Reynolds number for $q''_{eff}=32$ and 80 W/cm^2 and (*b*) comparisons of pressure drops for circular jets and slot jet

$=76.37$ W/cm^2 and $Q=4.51\times10^{-5}$ m^3/s, respectively. Overall, lower temperatures are achieved with the circular jets despite a significantly higher heat flux for the circular jets compared with the slot jet. Furthermore, far better axial temperature uniformity is evident in the temperature contours of the circular jets compared with the slot jet. These findings prove the circular-jet pattern provides superior cooling performance, albeit at the expense of greater pressure drop.

4 Two-Phase Heat Transfer Results

4.1 Boiling Curve Trends. Figures 9(*a*) and 9(*b*) show boiling curves for the four thermocouples in the copper block for circular jets at $Q=8.77\times10^{-6}$ m^3/s and $\Delta T_{sub}=68.2\,^{\circ}$C, and slot jets at $Q=7.15\times10^{-6}$ m^3/s and $\Delta T_{sub}=68.1\,^{\circ}$C, respectively. The slopes of the boiling curves are constant in the single-phase region for both jet configurations. CHF for both configurations commences at *tc*4, the most downstream thermocouple. CHF for the circular jets is 305 W/cm^2 compared with 243 W/cm^2 for the slot jet.

Figures 10(*a*) and 10(*b*) show the effects of subcooling on the boiling curve at $Q=2.15\times10^{-5}$ m^3/s for circular jets and $Q=3.53\times10^{-6}$ m^3/s for slot jets, respectively. The increase in subcooling delays the onset of boiling for both configurations. Notice

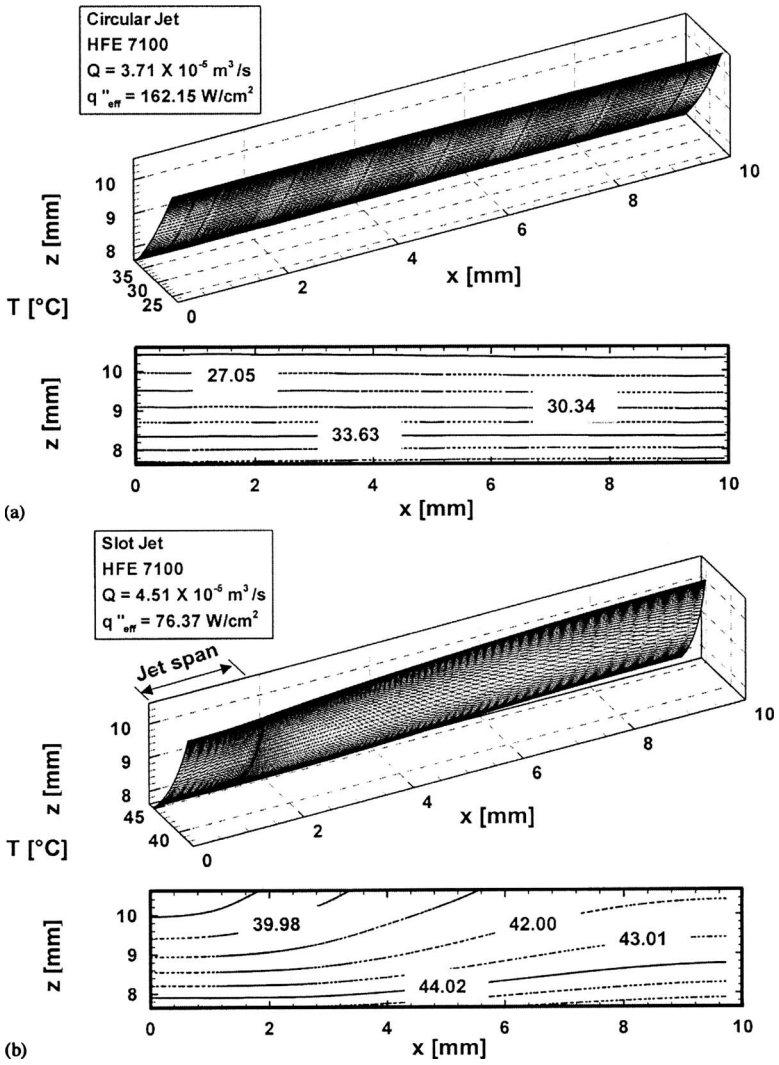

Fig. 8 Numerical predictions of microchannel sidewall temperature distribution for (*a*) circular jets at $q''_{eff}=162.15$ W/cm^2 and $Q=3.71\times10^{-5}$ m^3/s, and (*b*) slot jet at $q''_{eff}=76.37$ W/cm^2 and $Q=4.51\times10^{-5}$ m^3/s

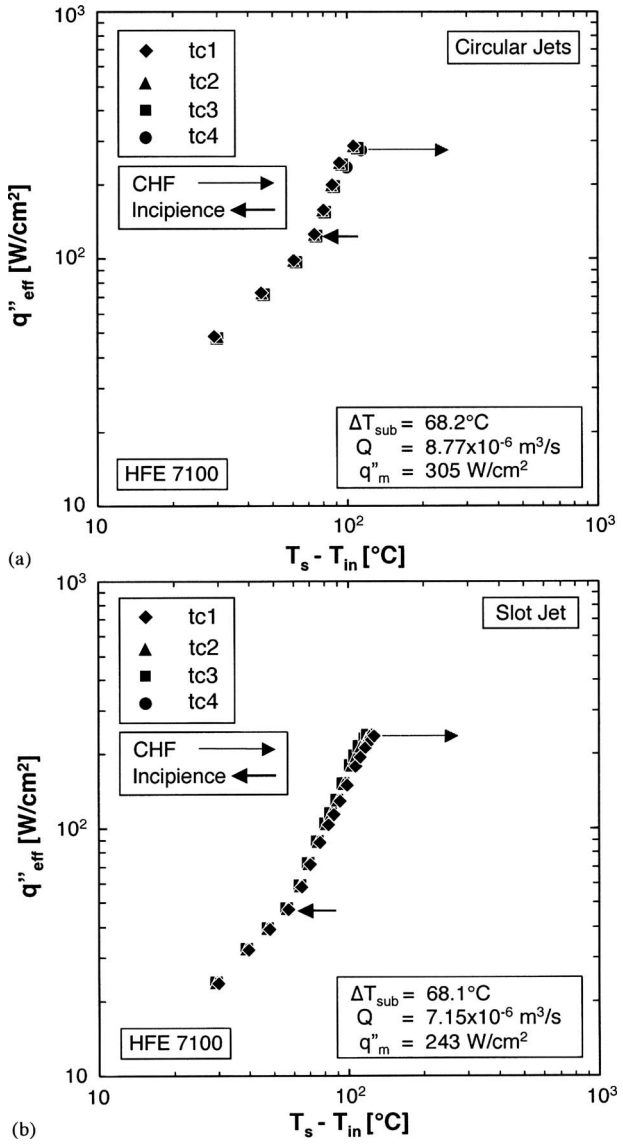

Fig. 9 Boiling curves measured at x_{tc1}, x_{tc2}, x_{tc3}, and x_{tc4} for (*a*) circular jets at ΔT_{sub}=68.2°C and Q=8.77×10^{-6} m^3/s, and (*b*) slot jet at ΔT_{sub}=68.1°C and Q=7.15×10^{-6} m^3/s

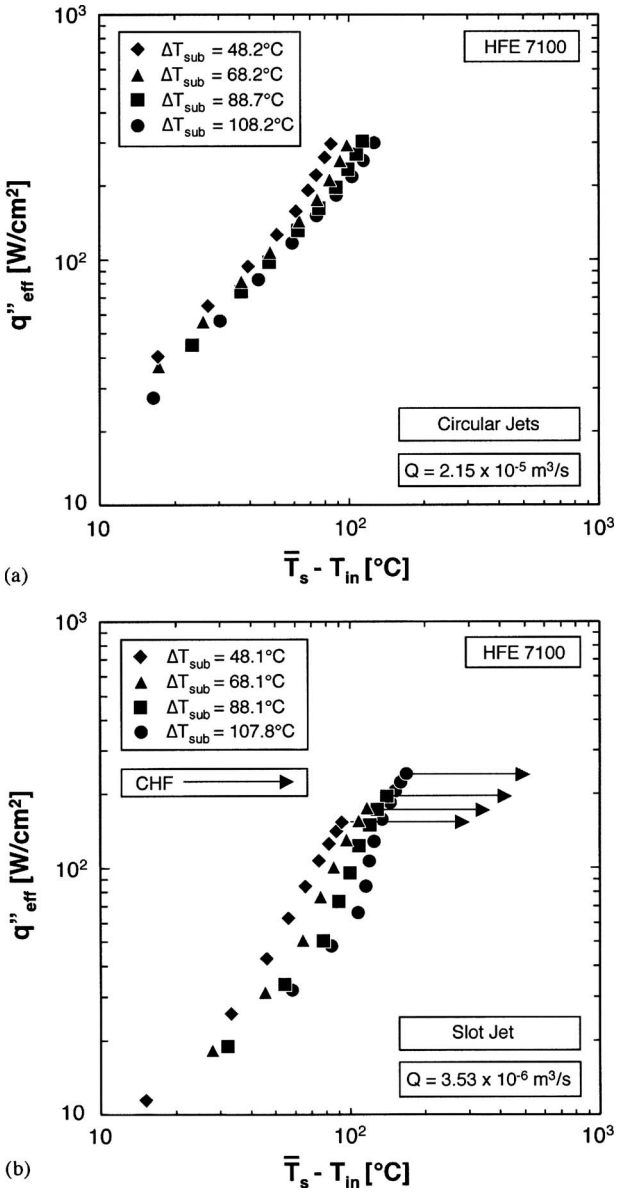

Fig. 10 Effects of subcooling on boiling curve for (*a*) circular jets at Q=2.15×10^{-5} m^3/s and (*b*) slot jet at Q=3.53 ×10^{-6} m^3/s

that CHF was not reached in some of the tests because these tests were terminated to protect the heater module against potential physical burnout. Figure 10(*b*) shows increasing the subcooling enhances CHF considerably for the slot jet. This enhancement is the result of the subcooled liquid's ability to absorb a substantial fraction of the supplied heat in the form of sensible heat prior to evaporation.

Figures 11(*a*) and 11(*b*) show the influence of flow rate on the boiling curve for the circular jets and slot jet, respectively. For both configurations, increasing the flow rate enhances the single-phase heat transfer coefficient and delays the onset of boiling. Data appear to converge in the nucleate boiling region. CHF increases appreciably with increasing flow rate, evidenced by the extended nucleate boiling region at higher flow rates.

Overall, Figs. 9–11 demonstrate that the circular-jet pattern provides significantly better cooling performance compared with the slot-jet pattern. This difference may be explained by drastic differences in the mechanisms of bubble production and growth along the microchannel for the circular jets and slot jet, as illustrated in Fig. 12(*a*) and 12(*b*), respectively. With the circular jets, liquid fed into the microchannel from the first jet (closest to the center of the microchannel) undergoes gradual bubble nucleation and growth. However, subcooled fluid from the second jet causes rapid condensation and collapse of upstream bubbles. This pattern of bubble growth and collapse is repeated along the microchannel with relatively mild net overall increase in vapor void fraction. On the other hand, coolant in the slot-jet case is supplied near the center of the microchannel and loses subcooling faster than the microjets, resulting in an appreciable increase in void fraction near the outlet. This loss of subcooling reduces CHF for the slot jet relative to the circular jets.

4.2 Nucleate Boiling Correlation. Mudawar and Wadsworth [27] showed the nucleate boiling heat transfer coefficient is independent of jet-impingement velocity. Ma and Bergles [28] showed increasing the subcooling causes a slight shift in nucleate boiling data toward lower wall superheat. Nucleate boiling data for the two hybrid cooling configurations are correlated using the following relations between heat flux and wall superheat,

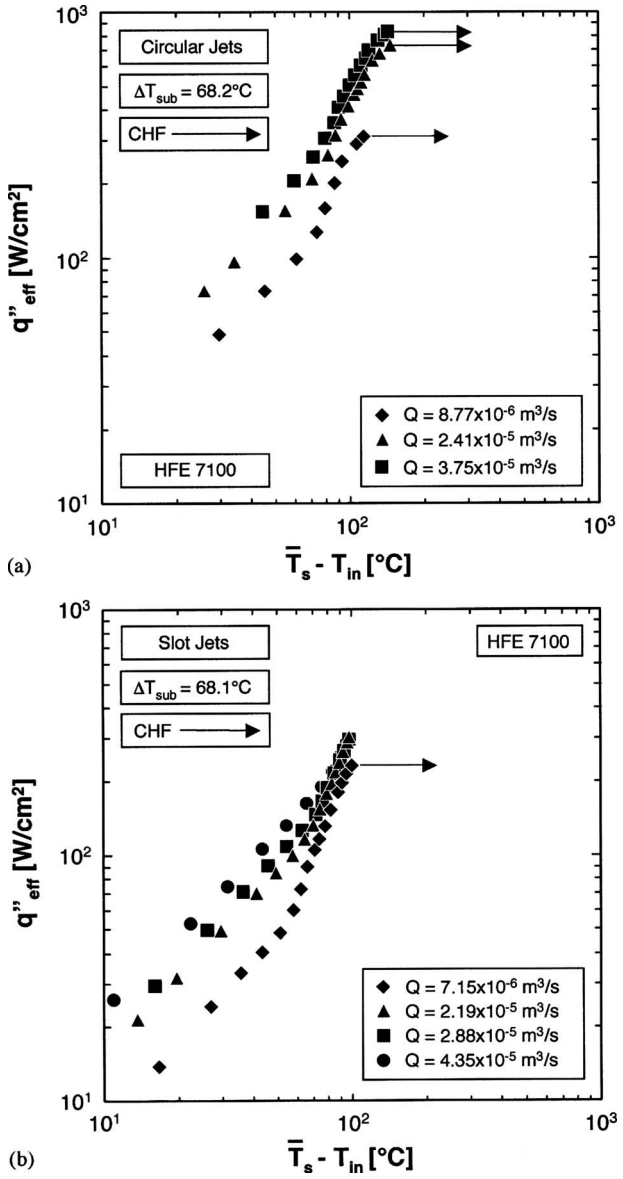

Fig. 11 Effects of flow rate on boiling curve for (*a*) circular jets at ΔT_{sub}=68.2°C and (*b*) slot jet at ΔT_{sub}=68.1°C

$$q''_{\text{eff}} = C(\bar{T}_s - T_{\text{sat}})^n \tag{1}$$

and

$$q''_{\text{eff}} = h(\bar{T}_s - T_{\text{in}}) = h[(\bar{T}_s - T_{\text{sat}}) + (T_{\text{sat}} - T_{\text{in}})] \tag{2}$$

Combining Eqs. (1) and (2) yields the following relation for the two-phase heat transfer coefficient:

$$h = \frac{q''_{\text{eff}}}{\left(\frac{q''_{\text{eff}}}{C}\right)^{1/n} + \Delta T_{\text{sub}}} \tag{3}$$

The empirical constants n and C in Eq. (3) are fitted with the experimental data. Interestingly, both hybrid configurations are fitted by the same correlation

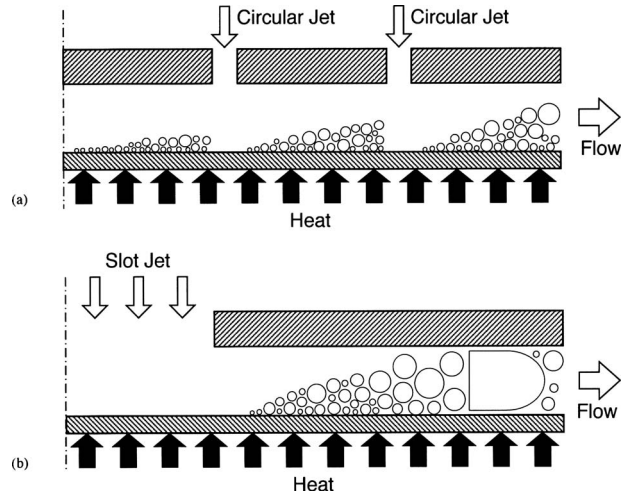

Fig. 12 Bubble growth and condensation inside hybrid module for (*a*) circular jets and (*b*) slot jet

$$h = \frac{q''_{\text{eff}}}{\left(\frac{q''_{\text{eff}}}{64.81}\right)^{1/3.252} + \Delta T_{\text{sub}}} \tag{4}$$

Figure 13 shows Eq. (4) is equally successful at predicting the two-phase heat transfer coefficient data for both configurations, evidenced by a mean absolute error of only 5.75%.

4.3 Upper Cooling Performance. As indicated earlier, some of the tests were terminated before reaching CHF in order to protect the costly test module against potential physical burnout. However, once a sufficient database was acquired for both the circular-jet and slot-jet patterns, a few additional tests were performed with the circular-jet pattern, which provided the more superior performance of the two configurations, to explore upper cooling limits. Figure 14 shows boiling curves for two such tests. These curves follow the previously mentioned trends of increasing jet velocity increasing both the single-phase heat transfer coeffi-

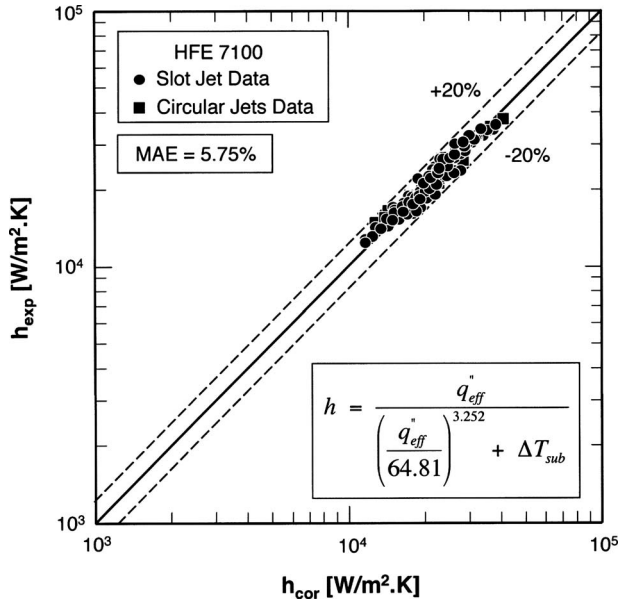

Fig. 13 Comparison of predictions of two-phase heat transfer coefficient correlation with HFE 7100 data for circular jets and slot jet

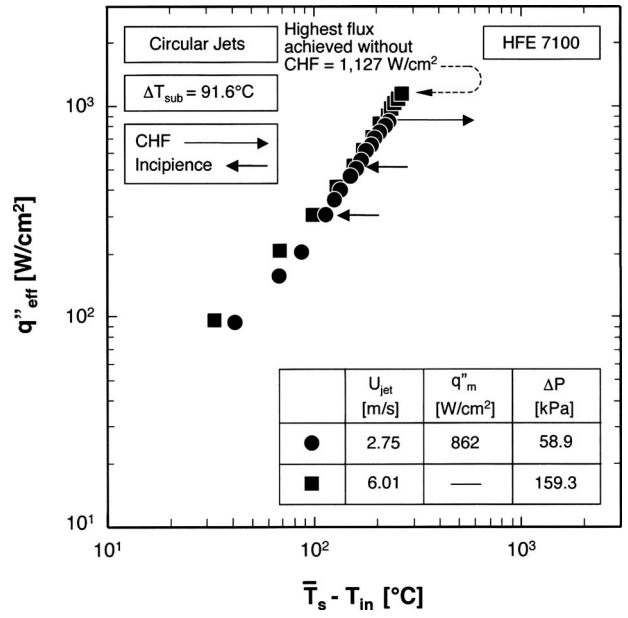

Fig. 14 Boiling curves for circular jets with U_{jet}=2.75 m/s and U_{jet}=6.01 m/s

cient and CHF, and the convergence of data for different velocities in the nucleate boiling region. Surprisingly, the higher jet velocity enabled the dissipation of an unprecedented heat flux of 1127 W/cm^2. This test was terminated at this heat flux without incurring CHF. These results demonstrate the enormous cooling potential of the hybrid cooling scheme utilizing the circular-jet pattern.

5 Conclusions

This study explored the implementation of hybrid cooling schemes that combine the attributes of microchannel flow and jet impingement. Two different jet configurations were examined using HFE 7100 as working fluid. In the first, the coolant is supplied to each microchannel through an array of circular jets. A single slot jet is utilized in the second configuration to supply the coolant into the microchannel. Both configurations were examined for their potential in achieving very high heat transfer coefficients and minimizing wall temperature gradients. The single-phase performance of each hybrid configuration was investigated both numerically and experimentally, while two-phase performance was examined experimentally. A few tests were performed in pursuit of upper cooling limits. Key findings from the study are as follows:

1. Microchannel height has a strong bearing on single-phase cooling performance and wall temperature uniformity for circular jets. Very small microchannel heights allow the jets to penetrate the microchannel flow but decrease the microchannel's heat transfer area. On the other hand, very large microchannel heights compromise cooling performance by preventing the jets from impacting the wall. Numerical 3D simulation using the standard two-equation k-ε turbulence model is quite accurate in predicting cooling performance and effective at identifying optimum microchannel height.
2. In the single-phase region for both jet configurations, increasing jet Reynolds number decreases surface temperature, while increasing the heat flux increases both the surface temperature and temperature gradients. Overall, circular jets provide the more superior cooling performance at the expense of greater pressure drop.
3. For both configurations, increasing the coolant's flow rate delays the onset of boiling and increases CHF. Increasing the subcooling increases CHF considerably by enabling the liquid to absorb an appreciable fraction of the supplied heat in the form of sensible energy prior to evaporation. A two-phase heat transfer coefficient correlation is developed that is equally successful for both jet configurations.
4. The two-phase cooling performance of the circular-jet pattern is superior to that of the slot-jet pattern, especially in terms of high-flux dissipation. Differences in cooling performance between the two patterns are the result of drastically different mechanisms of void fraction development along the microchannel. The superior performance of the circular pattern is realized with a repeated pattern of bubble growth and collapse between jets that nets only a mild overall increase in vapor void fraction. Cooling fluxes as high as 1127 W/cm^2 were achieved with the circular-jet pattern without incurring CHF.

Acknowledgment

The authors are grateful for the support of the Office of Naval Research (ONR).

Nomenclature

A_t = top test surface area of copper block (1.0 $\times$ 2.0 cm^2)
C = empirical constant
D_{jet} = diameter of microcircular jet
H = height of unit cell
H_{ch} = height of microchannel
H_{jet} = height (length) of microjet
H_{th} = height from unit cell's bottom boundary to thermocouple hole
H_w = height from unit cell's bottom boundary to bottom wall of microchannel
h = two-phase convective heat transfer coefficient, $q''_{eff}/(\bar{T}_s - T_{in})$
h_{fg} = latent heat of vaporization
L = length of unit cell (also length of microchannel)
L_1, L_2, L_3, and L_4 = distance between thermocouple holes
L_{jet} = circular-jet pitch
L_{jet1} = length of slot jet
L_{out} = length of microchannel downstream of slot jet
n = empirical constant
P = pressure
ΔP = pressure drop across test module
P_W = electrical power input to copper block
Q = volumetric flow rate
q''_{eff} = effective heat flux based on top test surface area of copper block, P_W/A_t
q''_m = critical heat flux based on top test surface area (A_t) of copper block
Re_{jet} = jet Reynolds number, $\rho_f U_{jet} D_{jet}/\mu_f$ or $\rho_f U_{jet}(2W_{jet})/\mu_f$
T = temperature
T_{in} = test module's inlet temperature
T_s = microchannel's bottom wall temperature
$\bar{T}_s$ = mean temperature of microchannel's bottom wall
T_{tci} = temperature measured by thermocouple tci (i = 1–4)
ΔT_{sub} = subcooling, $T_{sat} - T_{in}$
U_{jet} = mean jet velocity
W = width of unit cell
W_{ch} = width of microchannel
W_{jet} = width of slot jet

W_w = half-width of copper wall separating microchannels
x, y, and z = Cartesian coordinates

Greek Symbols

μ = viscosity
ρ = density
σ = surface tension

Subscripts

ch = channel
cor = correlation
exp = experimental, measured
in = test module's inlet
jet = jet
s = bottom wall of microchannel
sat = saturation
sub = subcooling
tci = thermocouple (i=1–4)
th = thermocouple

References

[1] Mudawar, I., 2001, "Assessment of High-Heat-Flux Thermal Management Schemes," IEEE Trans. Compon. Packag. Technol., **24**, pp. 122–141.
[2] Tuckerman, D. B., and Pease, R. F. W., 1981, "High-Performance Heat Sinking for VLSI," IEEE Electron Device Lett., **2**, pp. 126–129.
[3] Peng, X. F., and Wang, B. X., 1993, "Forced Convection and Flow Boiling Heat Transfer for Liquid Flowing Through Microchannels," Int. J. Heat Mass Transfer, **36**, pp. 3421–3427.
[4] Bowers, M. B., and Mudawar, I., 1994, "High Flux Boiling in Low Flow Rate, Low Pressure Drop Mini-Channel and Micro-Channel Heat Sinks," Int. J. Heat Mass Transfer, **37**, pp. 321–332.
[5] Qu, W., and Mudawar, I., 2004, "Measurement and Correlation of Critical Heat Flux in Two-Phase Micro-Channel Heat Sinks," Int. J. Heat Mass Transfer, **47**, pp. 2045–2059.
[6] Lelea, D., Nishio, S., and Takano, K., 2004, "The Experimental Research on Micro-Tube Heat Transfer and Fluid Flow of Distilled Water," Int. J. Heat Mass Transfer, **47**, pp. 2817–2830.
[7] Lee, J., and Mudawar, I., 2005, "Two-Phase Flow in High-Heat-Flux Micro-Channel Heat Sink for Refrigeration Cooling Applications: Part I—Pressure Drop Characteristics," Int. J. Heat Mass Transfer, **48**, pp. 928–940.
[8] Kim, S. J., and Kim, D., 1999, "Forced Convection in Microstructures for Electronic Equipment Cooling," ASME J. Heat Transfer, **121**, pp. 639–645.
[9] Fedorov, A. G., and Viskanta, R., 2000, "Three-Dimensional Conjugate Heat Transfer in the Microchannel Heat Sink for Electronic Packaging," Int. J. Heat Mass Transfer, **43**, pp. 399–415.
[10] Qu, W., and Mudawar, I., 2002, "Experimental and Numerical Study of Pressure Drop and Heat Transfer in a Single-Phase Micro-Channel Heat Sink," Int. J. Heat Mass Transfer, **45**, pp. 2549–2565.
[11] Craft, T. J., Graham, L. J. W., and Lauder, B. E., 1993, "Impinging Jet Studies for Turbulence Model Assessment—II. An Examination of the Performance of Four Turbulence Models," Int. J. Heat Mass Transfer, **36**, pp. 2685–2697.
[12] Park, T. H., Choi, H. G., Yoo, J. Y., and Kim, S. J., 2003, "Streamline Upwind Numerical Simulation of Two-Dimensional Confined Impinging Slot Jets," Int. J. Heat Mass Transfer, **46**, pp. 251–262.
[13] Baydar, E., and Ozmen, Y., 2005, "An Experimental and Numerical Investigation on a Confined Impinging Air Jet at High Reynolds Numbers," Appl. Therm. Eng., **25**, pp. 409–421.
[14] Martin, H., 1977, "Heat and Mass Transfer Between Impinging Gas Jets and Solid Surfaces," Adv. Heat Transfer, **13**, pp. 1–60.
[15] Jiji, L. M., and Dagan, Z., 1987, *Experimental Investigation of Single-Phase Multi-Jet Impingement Cooling of Array of Microelectronic Heat Sources*, Proc. Int. Symp. on Cooling Technology for Electronic Equipment, Honolulu, HI, pp. 265–283.
[16] Monde, M., 1987, "Critical Heat Flux in Saturated Forced Convection Boiling on a Heated Disk With an Impinging Jet," ASME J. Heat Transfer, **109**, pp. 991–996.
[17] Wadsworth, D. C., and Mudawar, I., 1990, "Cooling of a Multichip Electronic Module by Means of Confined Two-Dimensional Jets of Dielectric Liquid," ASME J. Heat Transfer, **112**, pp. 891–898.
[18] Estes, K. A., and Mudawar, I., 1995, "Comparison of Two-Phase Electronic Cooling Using Free Jets and Sprays," ASME J. Electron. Packag., **117**, pp. 323–332.
[19] Wolf, D. H., Incropera, F. P., and Viskanta, R., 1996, "Local Jet Impingement Boiling Heat Transfer," Int. J. Heat Mass Transfer, **39**, pp. 1395–1406.
[20] Johns, M. E., and Mudawar, I., 1996, "An Ultra-High Power Two-Phase Jet-Impingement Avionic Clamshell Module," ASME J. Electron. Packag., **118**, pp. 264–270.
[21] Monde, M., and Mitsutake, Y., 1996, "Critical Heat Flux in Forced Convective Subcooled Boiling With Multiple Impinging Jets," ASME J. Heat Transfer, **118**, pp. 241–243.
[22] Sung, M. K., and Mudawar, I., 2006, "Experimental and Numerical Investigation of Single-Phase Heat Transfer Using a Hybrid Jet Impingement/Micro-Channel Cooling Scheme," Int. J. Heat Mass Transfer, **49**, pp. 682–694.
[23] Sung, M. K., and Mudawar, I., 2008, "Single-Phase Hybrid Micro-Channel/Jet Impingement Cooling," Int. J. Heat Mass Transfer, **51**, pp. 4342–4352.
[24] 2005, Fluent 6.2.16, User's Guide, Fluent Inc., NH, Lebanon.
[25] 2006, Gambit 2.2.30, User's Guide, Fluent Inc., NH, Lebanon.
[26] Launder, B. E., and Spalding, D. B., 1974, "The Numerical Computation of Turbulent Flows," Comput. Methods Appl. Mech. Eng., **3**, pp. 269–289.
[27] Mudawar, I., and Wadsworth, D. C., 1991, "Critical Heat Flux From a Simulated Chip to a Confined Rectangular Impinging Jet of Dielectric Liquid," Int. J. Heat Mass Transfer, **34**, pp. 1465–1479.
[28] Ma, C. F., and Bergles, A. E., 1986, "Jet Impingement Nucleate Boiling," Int. J. Heat Mass Transfer, **29**, pp. 1095–1101.